



Article

Anisotropic Optical Response of WTe₂ Single Crystals Studied by Ellipsometric Analysis

Krastyo Buchkov^{1,2} , Rosen Todorov¹, Penka Terziyska², Marin Gospodinov², Velichka Strijkova¹ ,
Dimitre Dimitrov^{1,2,*} and Vera Marinova^{1,*}

¹ Institute of Optical Materials and Technologies, Bulgarian Academy of Sciences, 1113 Sofia, Bulgaria; k.buchkov@hotmail.com (K.B.); rntodorov@abv.bg (R.T.); vily@iomt.bas.bg (V.S.)

² Institute of Solid State Physics, Bulgarian Academy of Sciences, 1784 Sofia, Bulgaria; penka.terziyska@gmail.com (P.T.); maringospodinov@abv.bg (M.G.)

* Correspondence: dzdimitrov@issp.bas.bg (D.D.); vmarinova@iomt.bas.bg (V.M.)

Abstract: In this paper we report the crystal growth conditions and optical anisotropy properties of Tungsten ditelluride (WTe₂) single crystals. The chemical vapor transport (CVT) method was used for the synthesis of large WTe₂ crystals with high crystallinity and surface quality. These were structurally and morphologically characterized by means of X-ray diffraction, optical profilometry and Raman spectroscopy. Through spectroscopic ellipsometry analysis, based on the Tauc–Lorentz model, we identified a high refractive index value (~4) and distinct tri-axial anisotropic behavior of the optical constants, which opens prospects for surface plasmon activity, revealed by the dielectric function. The anisotropic physical nature of WTe₂ shows practical potential for low-loss light modulation at the 2D nanoscale level.

Keywords: WTe₂; chemical vapor transport; XRD; Raman spectroscopy; spectroscopic ellipsometry



Citation: Buchkov, K.; Todorov, R.; Terziyska, P.; Gospodinov, M.; Strijkova, V.; Dimitrov, D.; Marinova, V. Anisotropic Optical Response of WTe₂ Single Crystals Studied by Ellipsometric Analysis. *Nanomaterials* **2021**, *11*, 2262. <https://doi.org/10.3390/nano11092262>

Academic Editors: Ana Maria Diez-Pascual, Antonio Di Bartolomeo, Guanying Chen and Jorge Pasán

Received: 17 June 2021

Accepted: 27 August 2021

Published: 31 August 2021

Publisher's Note: MDPI stays neutral with regard to jurisdictional claims in published maps and institutional affiliations.



Copyright: © 2021 by the authors. Licensee MDPI, Basel, Switzerland. This article is an open access article distributed under the terms and conditions of the Creative Commons Attribution (CC BY) license (<https://creativecommons.org/licenses/by/4.0/>).

1. Introduction

Tungsten ditelluride (WTe₂) is one of the most prominent layered transition metal dichalcogenide (TMD) materials, with diverse and complex physical properties, providing many unexplored research directions in both fundamental and applied materials science [1–3]. These are related to its unique type-II Weyl fermion nature; it is a topological semimetal in which both edge and 2D bulk metallic states exist, with the potential to be modified in a 2D topological insulator using various control options such as temperature, magnetic, electric and optical fields, pressure and strain, electrostatic gating and bias voltages [4–8].

The origin of the electronic band nature of WTe₂ [9] is a distinct orthorhombic 1T' (distorted) crystal structure, also known as the T_d phase—in contrast to the usually observed 2H and 1T variants in TMD-class materials. The W atoms are arranged in a distorted triangular lattice (between the consecutive 180°-rotated Te layers) with the formation of quasi(1D) W-W chains, leading to significant tri-axial anisotropy [10,11] of the electrical, magnetic, thermal and optical properties.

The complexity of WTe₂ physics also includes unique phenomena such as titanite (non-saturating) magnetoresistance [12], “negative” magnetoresistivity [13], a room temperature ferroelectric semimetal state [14], superconductivity [15] and a diverse set of electronic and quantum topological effects in 2D form, such as the temperature-induced Lifshitz transition [16], the linear Nernst effect [17] and the observation of the quantum spin Hall effect up to 100 K [18].

In the photonics field, 2D layered materials [19,20], and particularly the TMD family [21], offer many options for functional light control, strong light–matter interaction effects and reduced optical losses. We have to emphasize their notable optical anisotropy [22,23],

which is a key factor in light manipulation due to the bi/trirefringence and di/trichroism effects [24], which result in spatial and polarization separation, enabling a virtually unlimited platform for the realization of the next generation (4G) of planar optics.

For the TMD materials group, the large in-plane vs. out-of-plane anisotropy arises from different interlayer (weak van der Waals bonds) and intralayer strong atomic interactions due to ionic/covalent bonding. Consequently, record birefringence values were observed in MoS₂ [22], as high as $\Delta n \sim 1.5$ in the infrared and $\Delta n \sim 3$ in the visible spectral range. Currently, such high birefringence is offered by artificially designed metamaterials and metasurfaces; however, the fabrication processes and optical losses are the main challenges [25]. For example, inorganic solids and liquid crystals possess relatively small birefringence, typically up to 0.4 [26,27]. At the same time, several 2D materials such as “black phosphorous” [28] and the monochalcogenides family [29] display exceptional tri-axial optical anisotropy (theoretically predicted for ReSe₂ [30] (isostructural to WTe₂)).

In this context, WTe₂ is intensively studied with comprehensive spectroscopic investigations of the electronic band structure. The uniaxial shaped Fermi surface and inter-band transitions lead to significant intrinsic anisotropy [10,11,31,32] and, together with the 2D layered topological [33–36] properties, expand the list of degrees of freedom for the optical control and detection of the light wave-vector, the intensity, polarization, phase, frequency, nanoscale confinement and collective charge excitations (plasmonic activity) [37–41]. Optical absorber devices based on WTe₂ have already been developed as part of prototype ultrafast laser systems [42–44].

Moreover, the synthesis of WTe₂ is rather difficult due to low chemical reactivity between W and Te compounds. The production of ultrathin WTe₂ nanostructures via conventional thin-film deposition techniques such as chemical vapor deposition [45] and molecular beam epitaxy [46] is quite limited and currently realized in a mono- or few-layered (2D) form only at μm -scale clusters. Alternatively, the unique properties of WTe₂ at the nanoscale level are mainly accessible via exfoliation techniques, which makes the development of the bulk crystal growth process of prime importance.

Following the above-noted research trends and perspectives, here we present an unexplored view of the tri-axial anisotropic optical response of WTe₂ (cleaved high-quality single crystals) via a study of reflection ellipsometry. The paper is structured as follows: we first report extended details about the growth process of high-quality WTe₂ single crystals using the CVT technique. Next, we briefly present the WTe₂ structure confirmed by X-ray diffraction (XRD), optical profilometry and Raman analysis. As a final point, we discuss the behavior of the main optical constants and dielectric function components, depending on the crystallographic orientations.

2. Materials, Methods and Experimental Details

2.1. WTe₂ Crystal Growth Procedure Using the CVT Method

WTe₂ single crystals were grown using the chemical vapor transport (CVT) method, a conventional approach for the preparation of TMD materials [47,48]. The preliminary stages start with the mixing of W and Te precursors (high purity > 5 N) for a solid-state reaction synthesis at 725 °C (72 h) in an evacuated ampule ($\sim 10^{-4}$ torr), followed by additional powdering and homogenization steps. The pre-sintered WTe₂ material and an appropriate amount of Br (a volatile transport agent to mediate the growth process—3 mg/mL volume) were sealed in evacuated CVT quartz ampule. The ampule was designed with enlarged diameter, considering the geometry of the dual-zone furnace thermal gradient, the W/Te phase diagram [49], the precursor amounts required to maintain the optimal thermal equilibrium and the crystallization conditions for the formation of large-sized WTe₂ crystals. Finally, the ampule was positioned in separate thermal gradient zones of 780 °C and 680 °C and the growth process was maintained for a maximally extended period—approximately 190 h. The CVT process is schematically visualized in Figure 1.

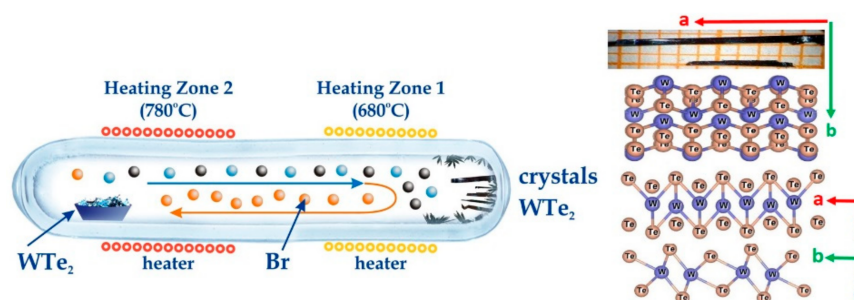


Figure 1. Schematic of the CVT crystal growth process (left). Optical images of the largest acquired samples (top right) with the crystallographic axis orientations and a visual representation of the layered crystal structure of WTe_2 (using Vesta).

The obtained WTe_2 crystal flakes had an elongated rectangular geometry as a result of the high a/b orthorhombicity ratio. Their size varied from mm to cm, with a flat and shiny metallic surface, and their thickness was usually under $100\ \mu\text{m}$. The residual traces of Br transport contaminations were removed via dynamic evacuation for 24 h, followed by a simple surface cleaning procedure of immersing the crystals subsequently in acetone (5 min) and in isopropanol (5 min).

WTe_2 is vulnerable to ambient conditions, with rapid and irreversible surface oxidation [14,50,51]. Therefore, the samples were stored in GloveBox system (under inert atmosphere with oxygen/moisture levels less than 1 ppm) and exposed only during the experimental investigations. In order to provide a more unperturbed view of the intrinsic optical properties of the material, the crystal samples were cleaved with a Nitto tape to attain a fresh surface just before the ellipsometric experiments.

2.2. Characterization Instruments and Techniques

The crystal structure of powdered WTe_2 crystals were analyzed using XRD over the 2θ range of 5.3° to 80° /constant step of 0.02° , using a Cu K_α “D8 Advance” Bruker (Karlsruhe, Germany) diffractometer equipped with a LynxEye detector. The structural data were identified with Diffracplus EVA using the ICDD-PDF2 crystallographic database. The WTe_2 crystal structure was presented using Vesta ver. 3.4.8 [52] structural analysis and visualization software.

The surface morphology was investigated in several sectors using an optical profilometry/metrology system, Zeta-20, from Zeta Instruments. The Raman spectra were recorded (backscattering geometry) using a HORIBA Jobin Yvon Labram HR visible spectrometer with a He-Ne laser (633-nm excitation line) and a Peltier-cooled charge-coupled device (CCD) detector.

The ellipsometry measurements were performed in reflection mode using a J.A Woollam (Lincoln, NE, USA) M2000D rotating-compensator spectroscopic ellipsometer in the spectral range from 193 nm to 1000 nm.

Complete EASE software (J.A Woollam) was used to measure and model the spectra of the ellipsometric Ψ and Δ parameters. The analysis procedure is similar to that described in the case of a biaxial microcrystal of MoS_2 [22]. As a last step in fitting the measured spectra of ψ (the amplitude ratio) and Δ (phase difference), we determine the Euler angles—the rotation of the crystal axes (n_x, n_y, n_z) relative to the experiment coordinate system, denoted by N, S and P (where N is the normal to the surface of the sample and S and P are the directions perpendicular and in the plane of incidence of light). The values obtained for the Euler angles were less than 1.8° .

For the specific investigation and analysis (XRD, Raman spectroscopy and Ellipsometry), several high-quality WTe_2 crystal flakes were selected (using optical microscopy and profilometry, Appendix A) depending on their defect-less surface quality. Due to their fragile and delicate morphology (resembling an ultrathin foil), the samples were care-

fully attached to a glass substrate to ensure the effective implementation of ellipsometric experiments.

3. Discussion and Results

3.1. XRD Analysis

The crystal structure of the selected samples was characterized using X-ray diffraction. Powder XRD analysis was used and the results are presented in Figure 2. The phase identification did not detect crystalline impurities. The cell parameters were determined to be: $a = 6.278(6)$ Å, $b = 3.483(5)$ Å and $c = 14.054(8)$ Å, which are typical for the designated orthorhombic space group: Pmn21, No. 31 [1,53]. The main diffraction peak [002] was detected at 12.60° 2θ degrees, whereas, due to its layered structure, the other characteristic peaks [004], [006], [008] and [0010] were detected with minor intensity. The preferential [00 \uparrow] crystallographic orientation was a fine confirmation of the highly crystalline nature of the samples and the efficiency of CVT growth.

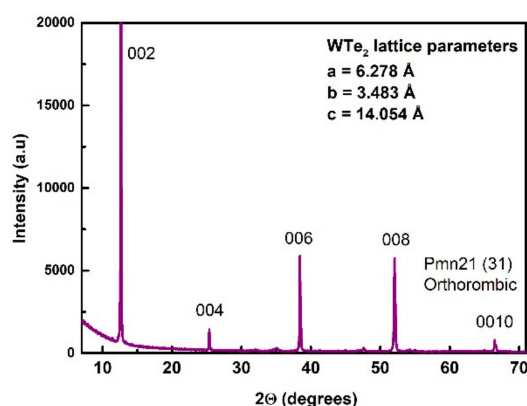


Figure 2. XRD analysis of WTe₂ sample with the main identified peaks of the preferential crystallographic orientation.

3.2. Raman Spectroscopy

In addition to the XRD, the single crystal structural quality was also indirectly assessed by means of Raman spectroscopy analysis. Raman peaks (presented in Figure 3.) typical for pure WTe₂ are identified as $A_1^9 \sim 210$ cm⁻¹, $A_1^7 \sim 163$ cm⁻¹, $A_1^4 \sim 132$ cm⁻¹, $A_1^3 \sim 111$ cm⁻¹ and $A_2 \sim 90$ cm⁻¹ [32,54]. Usually, narrow and intense Raman peak structures are related to the ability of the long-range propagation of Raman phonon modes through the crystal lattice, marking a high crystallinity level.

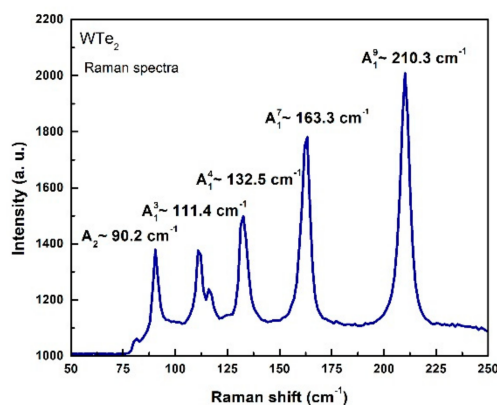


Figure 3. Raman spectrum of WTe₂ single crystal.

In addition, the crystal surface morphology and topology was investigated by means of optical profilometry (Figure A1) which verified the quality of the crystals selected for further cleaving and measurements.

3.3. Spectroscopic Ellipsometry

Optical anisotropy is a key factor in light manipulation due to the bi/trirefringence and di/trichroism effects, which results in spatial and polarization separation, enabling a new degree of freedom for next-generation photonic devices. Usually, for the anisotropy analysis of 2D TMD materials, the spectroscopic ellipsometry is applied in a transmission regime, considering the Jones matrix formalism and the finite (non-zero) values of the off-diagonal components [55,56] or using ellipsometric imaging [22] for thicker samples $\sim 1 \mu\text{m}$ due to the extreme signal dominance of the in-plane vs. out-of-plane optical components. However, due to the high values of the extinction coefficient $k(\lambda)$ of WTe_2 [38] (resulting in a small light penetration depth) and the narrow band gap, high optical absorption is expected for the wavelengths shorter than 2000 nm, which makes the use of transmission ellipsometry difficult in the visible and ultraviolet spectral regions. In addition, considering the noted limitations of WTe_2 synthesis in large-scale thin films, we applied reflection ellipsometry for the qualitative comparison and analysis of WTe_2 crystal flakes.

For the modeling of ellipsometric data, we used two different models. The initial analysis model assumed that the sample is an isotropic medium and two independent measurements were made at each incident light angle, considering the crystallographic orientation along the a - and b -axes through the elongated sample geometry, with the second measurement being performed by rotating the crystal to 90° . The dispersive refractive index $n(\lambda)$ and extinction coefficient $k(\lambda)$ were extracted from the direct inversion of the experimental ellipsometric ψ (the amplitude ratio) and Δ (phase difference) functions, associated with the p- and s-polarized light waves' characteristics.

The second approach was based (using the same experimental data set) on the assumption that the sample had an anisotropic triaxial crystal symmetry with different refractive indices along the three mutually perpendicular axes. Concerning the dielectric permittivity, we applied the Tauc–Lorentz model [57].

3.3.1. Basic Isotropic Model Approach: Refractive Index and Extinction Coefficient

For the applied isotropic model, the spectral behavior of the fundamental optical constants of WTe_2 crystals are presented at Figures 4 and 5. The refractive index $n(\lambda)$ for the cleaved WTe_2 crystal reached typically high values (~ 4) in both orientations (parallel to the a and b directions) with a specific double slope increasing with the wavelength (more rapidly in the ultraviolet region). Based on the observed $n(\lambda)$ values, WTe_2 can be categorized as a crystal with high-index dielectric class material (compared to other layered chalcogenides [58–60]), with a corresponding prospect for light absorption enhancement and directional light manipulation in photonic device applications.

The extinction coefficient $k(\lambda)$ also changed noticeably in both in-plane crystallographic directions (Figure 5). Different trends of the optical losses were observed in the investigated spectral area. Along the a -axis, the values of $k(\lambda)$ varied in the range of 1.5–3 with an observed minimum at $\sim 650 \text{ nm}$, whereas, for the b -axis, there was a gradual decrease from 3 to 1.

The performed optical measurements showed significant incident angle dependencies, resulting from different signal contributions along the orthogonal axes, mostly in the near-infrared region. Generally, this is also related to the typical anisotropic behavior of light propagation in low-symmetry layered materials [61].

Due to the ambient environment vulnerability of WTe_2 , which leads to the formation of a thin oxidation layer at the native surface, the possible effect of this on the optical constants was also studied. The optical response of the native WTe_2 crystal surface (before the cleaving) is presented in Figure A2A–D.

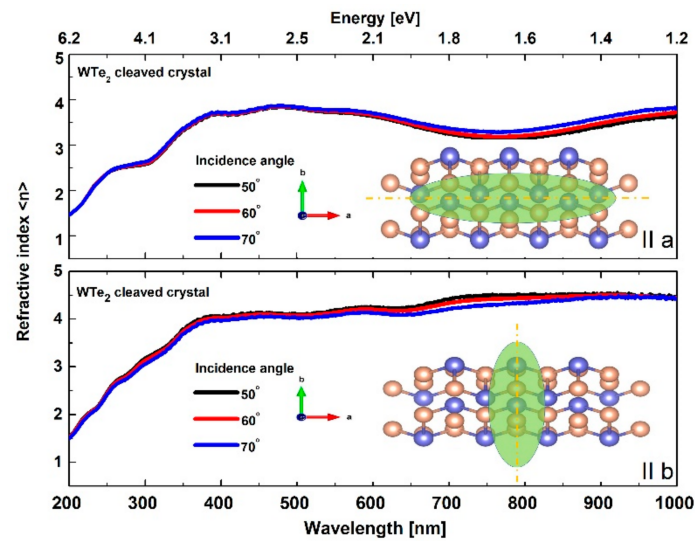


Figure 4. Spectral dependence of refractive index in the a and b directions for the cleaved WTe₂ crystal.

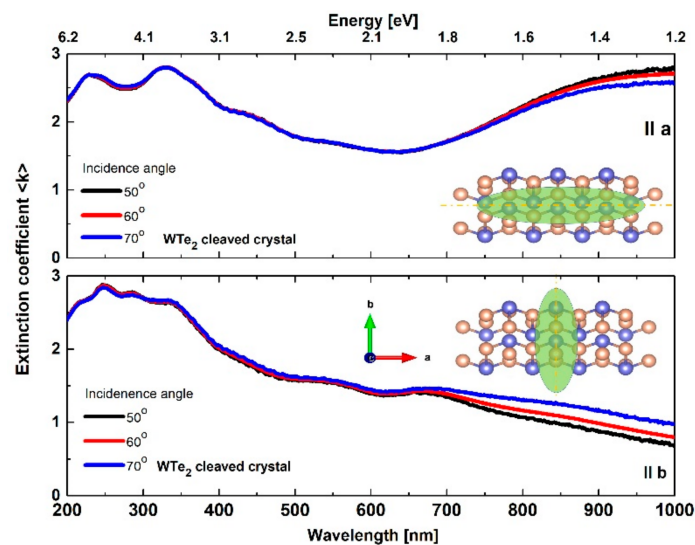


Figure 5. Spectral dependence of extinction coefficient in the a and b directions for the cleaved WTe₂ crystal.

3.3.2. Tauc–Lorentz Oscillator Model: Refractive Index and Extinction Coefficient

The notable tri-axial anisotropic behavior of WTe₂ was evident through numerical analysis using a Tauc–Lorentz oscillator model [56,57]. This method is generally applied for comprehensive ellipsometric investigations of the optical constants for layered TMD materials [22,61] and it is based on combined dielectric function parametrization using the Tauc Law and the Lorentzian oscillator model. For the particular tri-axial case of WTe₂, the dielectric tensor elements were described by the Tauc–Lorentz formalism considering different model parameters (fitting variables: E_g (optical band gap), Lorentz oscillator amplitude and energy, broadening factor) in the crystallographic directions. The number and the initial values of the frequencies of the Lorentz oscillators are determined by the local maxima observed in the spectra of the imaginary part of the complex dielectric constant obtained by the isotropic model. The results of the analysis showed that the minimum number of Lorentz oscillators required to obtain the best fit by the anisotropic model was three in the directions of the *a*- (at 1.07 eV, 2.98 eV and 5.01) and *b*-axes (at 2.87 eV, 3.84 eV and 4.77 eV) and two in the direction of the *c*-axis (at 4.65 eV and 5.84 eV).

The calculated dispersions, with significant qualitative and quantitative differences in the refractive index and extinction coefficient along the three (mutually perpendicular) axes, are presented in Figures 6 and 7. In addition, the relative (Figure 6, inset graph) in-plane vs. out-of-plane anisotropy ratio $\Delta n = \overline{n_{ab}} - n_c$ and birefringence was determined, reaching a maximal value ~ 1.5 in the studied visible and near-infrared region, along with the averaged in-plane $\overline{n_{ab}}$ response. For clarity, the data are presented in the visible/near-infrared spectral range due to the presence of resonant peaks in the ultraviolet region.

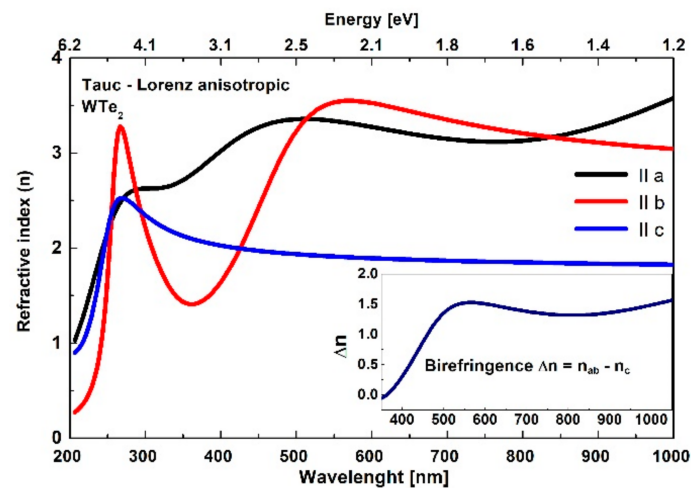


Figure 6. The tri-axial optical anisotropy of the WTe_2 refractive index in the frames of the Tauc-Lorentz model. Inset: relative birefringence in the visible/near-infrared region.

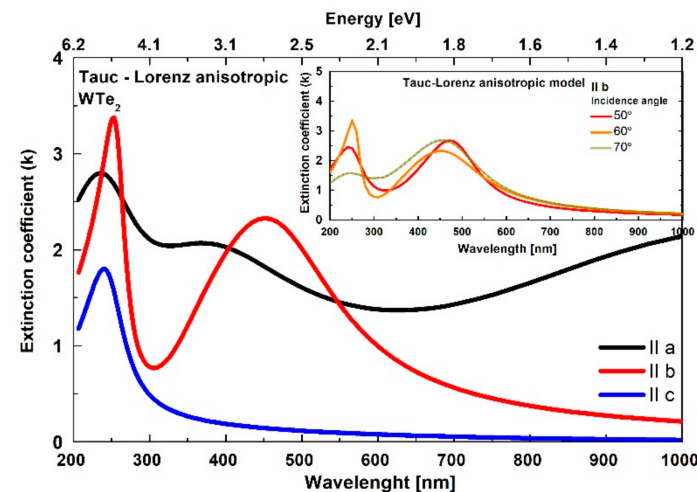


Figure 7. The triaxial optical anisotropy of the WTe_2 extinction coefficient in the frames of the Tauc-Lorentz model. Inset: incidence angle dependence of the extinction coefficient along the b -axis.

The extrapolated values of the optical band gap E_g in the a and b directions were 0.006 eV and 0.273 eV, respectively. The obtained value of 0.006 eV for the band gap along the a -axis suggests a metallic character of the crystal in this direction and high values of the extinction coefficient, whereas the larger values of E_g in the other direction suggest a decrease of $k(\lambda)$ values which become zero at a photon energy corresponding to the relevant band gap width. These results are in good agreement with the values determined by the density functional theory and first-principle calculations of the band structure reported in the literature [1,62].

The observed trirefringence and trichroism scenarios, with high unidirectional control of the light propagation, together with the high $n(\lambda)$ and low $k(\lambda)$ values (expected to be even higher for the exfoliated and thinner layers) are very promising for the development of

emerging nanophotonic devices. The Tauc–Lorentz model also showed significant optical constant differences calculated at different angles of light incidence, especially at shorter wavelengths, as shown in Figure 7 (inset), for the extinction coefficient along the *b*-axis.

We assume that this notable angle dependence difference is also related to the narrow light penetration depth expected for WTe₂. Considering the Beer–Lambert–Bouguer law: $T \sim e^{-\alpha d}$ (where T is transmittance, α is the absorption coefficient linked with the extinction coefficient $\alpha = 4\pi k/\lambda$ and d is the thickness of the sample), we can estimate the expected penetration depth for WTe₂ (presented in Figure A3, defined as $\alpha d \leq 1$).

The spectra of the extinction coefficient $k(\lambda)$ show that the penetration depth decreases with decreasing wavelength. The contribution from the *c*-axis decreases and, in this case, the simplistic isotropic model gives a better match in determining the refractive index and the extinction coefficient at the different incidence angles.

At longer wavelengths, the extinction coefficient decreases and consequently the penetration depth of the electromagnetic wave increases. Considering the axial influence, these will give a better match when counted at different angles. Naturally, the isotropic model does not take into account that the refractive index along the *c*-axis is different. Therefore, this leads to a difference in the optical constants (Figures 4 and 5) at wavelengths longer than 650 nm.

3.3.3. Dielectric Functions

In addition, based on the Tauc–Lorentz oscillator model and anisotropic analysis of the fundamental optical constants, the values of the real $\epsilon'(\lambda)$ and imaginary $\epsilon''(\lambda)$ dielectric function components were determined for the three crystallographic directions. For the cleaved WTe₂ crystal, the anisotropic trends are presented in Figure 8.

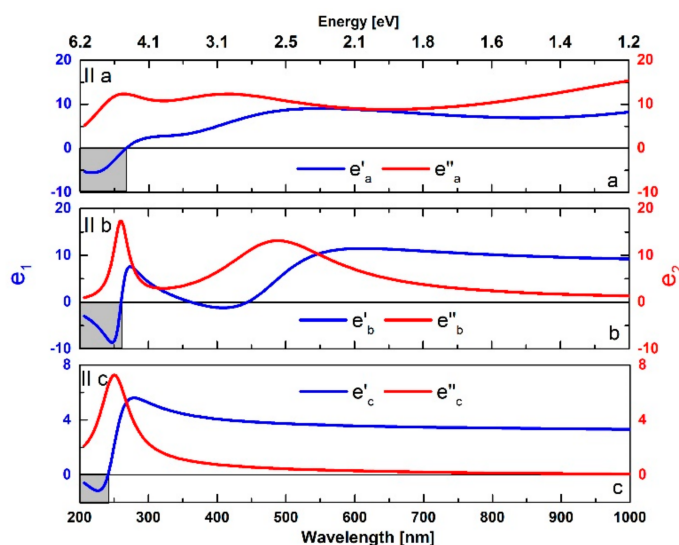


Figure 8. The tri-axial spectral behavior of the dielectric functions for WTe₂.

The main feature is the observation of negative values for $\epsilon'(\lambda)$ [37] in the ultraviolet/visible edge, revealing the presence of plasmonic resonances mediated by strong inter-band electronic transitions (as an alternative mechanism to the conventional collective excitation of the free charge carriers), typically observed in semi-metals (such as WTe₂), semiconductors and topological insulator materials [63].

Consequently, the sophisticated (low-symmetry Fermi surface) electronic band structure of Weyl (and Dirac) semi-metal materials also results in the observed notable anisotropy of the optical properties. The corresponding highly directional modulations of the carrier density and mobility also leads to the significant differences in the light polarizability and the dielectric functions along the *a*-, *b*- and *c*-axes in the case of WTe₂ single crystals.

4. Conclusions

In summary, large-sized WTe_2 crystals were grown by using the CVT method. Their crystal structure and morphology were characterized using XRD, optical profilometry and Raman spectroscopy, verifying their high crystallinity and surface quality. The optical response of cleaved WTe_2 crystal samples was analyzed by means of reflection spectroscopic ellipsometry. Two different data models were implemented—a simplistic isotropic and a Tauc–Lorentz based anisotropic model, revealing:

- High values of the refractive index (~ 4) were observed for both models, especially in the visible/near-infrared spectral range. The influence of the optical anisotropy was also well detected with the simplistic isotropic modeling, with observed distinct differences in the optical constants (n and k) depending on the in-plane crystallographic orientations.
- Identical anisotropic tendencies of the intrinsic WTe_2 spectral behavior were also observed for the native crystal surface, which is expected to be affected by the formation of an oxide surface layer (Appendix A).
- The calculated dispersions of the refractive index and extinction coefficient in the frames of the Tauc–Lorentz oscillator model indicate the tri-axial nature of the optical response.
- The extrapolated band gap values of 0.006 and 0.273 eV in the a and b directions, respectively, are in good agreement with those determined by energy band structure calculations in the literature.
- The real component of the dielectric function shows negative values, which also indicates surface plasmon polariton activity.

The observed anisotropic optical response emphasizes the practical prospects of WTe_2 for polarization-dependent light modulation and dielectric plasmonics in the innovative field of nanophotonics.

Author Contributions: Conceptualization, K.B., V.M. and R.T.; methodology, M.G., P.T., R.T. and V.S.; software, K.B.; validation, V.M., D.D. and M.G.; formal analysis, K.B., P.T. and R.T.; investigation, K.B., P.T., R.T., V.S. and V.M.; resources, D.D. and V.M.; data curation, K.B.; writing—original draft preparation, K.B.; writing—review and editing, K.B., V.M. and R.T.; visualization, K.B.; supervision, V.M.; project administration, V.M. and D.D.; funding acquisition, V.M. and D.D. All authors have read and agreed to the published version of the manuscript.

Funding: We acknowledge the funding of the European Commission via the TOCHA project H2020-FETPROACT-01-2018 under Grant Agreement No. 824140. V.M., D.D. and K.B. acknowledge the financial support by Bulgarian Science Fund under the projects KII-06-KOCT/1 and KII-06-KOCT/13. Research equipment of Distributed Research Infrastructure INFRAMAT, part of the Bulgarian National Roadmap for Research Infrastructures, supported by the Bulgarian Ministry of Education and Science was used in these investigations.

Institutional Review Board Statement: Not applicable.

Informed Consent Statement: Not applicable.

Data Availability Statement: The data presented in this study are available on request from the corresponding and leading authors.

Acknowledgments: The authors acknowledge the support of Daniela Kovacheva, Institute of Inorganic Chemistry, Bulgarian Academy of Sciences, Bulgaria for XRD measurements and Viktor Ivanov, Faculty of Physics, Sofia University for Raman spectroscopy analysis.

Conflicts of Interest: The authors declare no conflict of interest.

Appendix A

Appendix A.1. Optical Imaging and Profilometry

The crystal surface morphology and topology were investigated by means of optical profilometry. Several different sectors ($\sim 1000 \mu\text{m}^2$) (with sizes and areas comparable to the

laser ellipsometric spot) were scanned and the corresponding surface topology maps have been constructed—presented in Figure A1.

The data revealed that the surface (flatness level) is close to structural perfection even at a microscale level and this is an additional verification of the crystal quality, which was suitable for further exfoliation.

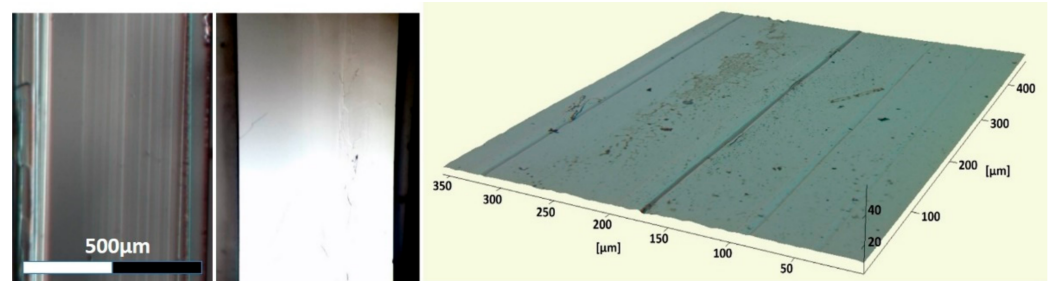


Figure A1. Optical images (under $\times 5$ magnification) of the selected WTe_2 crystal with the native surface (left), the cleaved surface (middle) and topographic profilometry (right) over the μm -scale sector of the native surface.

Appendix A.2. Ellipsometric Analysis: Native Surface and Light Penetration Depth

In our description of the experimental details, we noted the air exposure vulnerability of WTe_2 and the possible formation of a surface oxidation layer, and hence the cleaving procedure was performed immediately before the ellipsometry analysis.

Nevertheless, the potential influence of the oxidation layer on the complex refractive index components was also studied. The optical response of the native WTe_2 crystal surface (before cleaving) is presented in Figure A2A–D. Obviously, with the native surface, the samples showed similar qualitative behavior compared to the cleaved crystal and showed identical tendencies related to the intrinsic in-plane anisotropy of the material. It is important to note that, in this case, the influence of the incidence angle is much stronger and the splitting effects of the pseudo-optical constants are due to the in-plane/out-of-plane anisotropy.

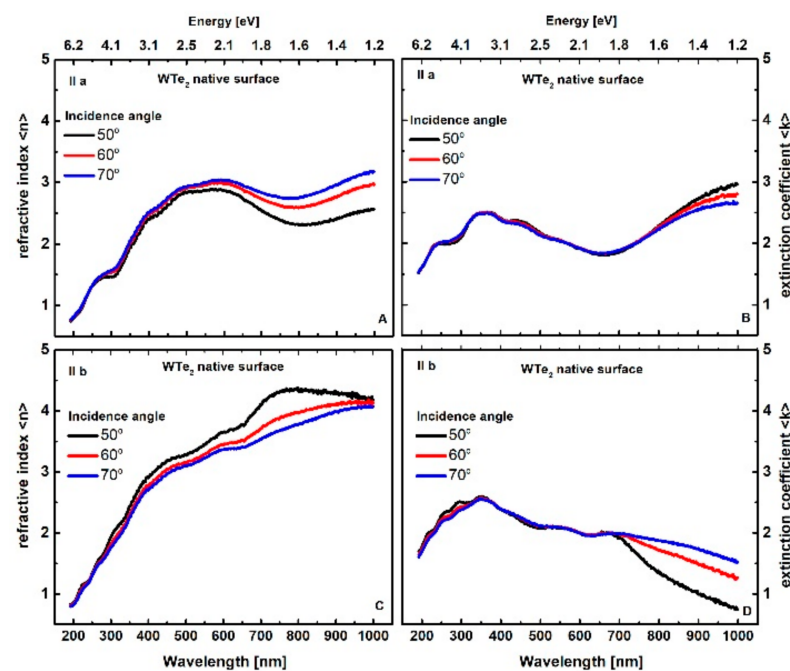


Figure A2. The refraction index (A,C) and extinction coefficient (B,D) obtained for the native surface of the WTe_2 single crystal.

The variation of the light penetration depth as a function of the wavelength is shown in Figure A3. The values of the extinction coefficient along the b -axis at 60° light incidence obtained by the anisotropic model were used for this calculation.

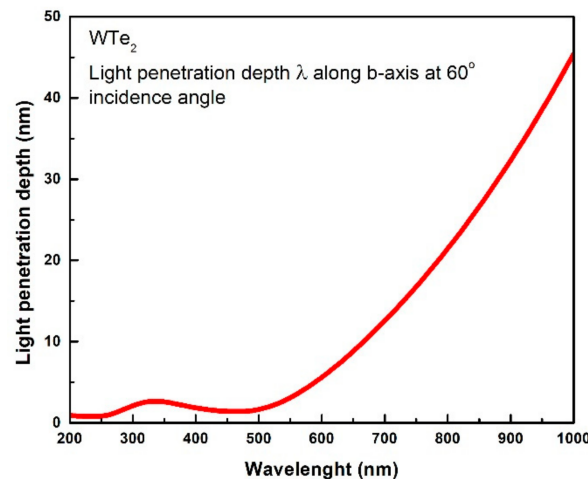


Figure A3. The spectral dependence of the light penetration depth along the b -axis at a 60° incidence angle.

References

- Lee, C.H.; Silva, E.C.; Calderin, L.; Nguyen, M.A.T.; Hollander, M.J.; Bersch, B.; Mallouk, T.E.; Robinson, J.A. Tungsten Ditelluride: A layered semimetal. *Sci. Rep.* **2015**, *5*, 10013. [\[CrossRef\]](#)
- Tian, W.; Yu, W.; Liu, X.; Wang, Y.; Shi, J. A Review of the Characteristics, Synthesis, and Thermodynamics of Type-II Weyl Semimetal WTe₂. *Materials* **2018**, *11*, 1185. [\[CrossRef\]](#)
- Pan, X.-C.; Wang, X.; Song, F.; Wang, B. The study on quantum material WTe₂. *Adv. Phys. X* **2018**, *3*, 1468279. [\[CrossRef\]](#)
- Das, P.K.; Di Sante, D.; Cilento, F.; Bigi, C.; Kopic, D.; Soranzio, D.; Sterzi, A.; Krieger, J.A.; Vobornik, I.; Fujii, J.; et al. Electronic properties of type-II Weyl semimetal WTe₂. A review perspective. *arXiv* **2018**, *1*, 014003.
- Jia, Z.Y.; Song, Y.H.; Li, X.B.; Ran, K.; Lu, P.; Zheng, H.J.; Zhu, X.Y.; Shi, Z.Q.; Sun, J.; Wen, J.; et al. Direct visualization of a two-dimensional topological insulator in the single-layer 1T'-WTe₂. *Phys. Rev. B* **2017**, *96*, 041108. [\[CrossRef\]](#)
- Fei, Z.; Palomaki, T.; Wu, S.; Zhao, W.; Cai, X.; Sun, B.; Nguyen, P.; Finney, J.; Xu, X.; Cobden, D.H. Edge conduction in monolayer WTe₂. *Nat. Phys.* **2017**, *13*, 677–682. [\[CrossRef\]](#)
- Xu, S.Y.; Ma, Q.; Shen, H.; Fatemi, V.; Wu, S.; Chang, T.R.; Chang, G.; Valdivia, A.M.M.; Chan, C.K.; Gibson, Q.D.; et al. Electrically switchable Berry curvature dipole in the monolayer topological insulator WTe₂. *Nat. Phys.* **2018**, *14*, 900–906. [\[CrossRef\]](#)
- Jelver, L.; Stradi, D.; Stokbro, K.; Olsen, T.; Jacobsen, K.W. Spontaneous breaking of time-reversal symmetry at the edges of 1T' monolayer transition metal dichalcogenides. *Phys. Rev. B* **2019**, *99*, 155420. [\[CrossRef\]](#)
- Augustin, J.; Eyert, V.; Böker, T.; Frentrup, W.; Dwelk, H.; Janowitz, C.; Manzke, R. Electronic band structure of the layered compound Td-WTe₂. *Phys. Rev. B Condens. Matter Mater. Phys.* **2000**, *62*, 10812–10823. [\[CrossRef\]](#)
- Zhang, Q.; Zhang, R.; Chen, J.; Shen, W.; An, C.; Hu, X.; Dong, M.; Liu, J.; Zhu, L. Remarkable electronic and optical anisotropy of layered 1T'-WTe₂ 2D materials. *Beilstein J. Nanotechnol.* **2019**, *10*, 1745–1753. [\[CrossRef\]](#)
- Frenzel, A.J.; Homes, C.C.; Gibson, Q.D.; Shao, Y.M.; Post, K.W.; Charnukha, A.; Cava, R.J.; Basov, D.N. Anisotropic electro-dynamics of type-II Weyl semimetal candidate WTe₂. *Phys. Rev. B* **2017**, *95*, 245140. [\[CrossRef\]](#)
- Ali, M.N.; Xiong, J.; Flynn, S.; Tao, J.; Gibson, Q.D.; Schoop, L.M.; Liang, T.; Haldolaarachchige, N.; Hirschberger, M.; Ong, N.P.; et al. Large, non-saturating magnetoresistance in WTe₂. *Nature* **2014**, *514*, 205–208. [\[CrossRef\]](#) [\[PubMed\]](#)
- Zhang, E.; Chen, R.; Huang, C.; Yu, J.; Zhang, K.; Wang, W.; Liu, S.; Ling, J.; Wan, X.; Lu, H.Z.; et al. Tunable Positive to Negative Magnetoresistance in Atomically Thin WTe₂. *Nano Lett.* **2017**, *17*, 878–885. [\[CrossRef\]](#)
- Sharma, P.; Xiang, F.X.; Shao, D.F.; Zhang, D.; Tsymbal, E.Y.; Hamilton, A.R.; Seidel, J. A room-temperature ferroelectric semimetal. *Sci. Adv.* **2019**, *5*, eaax5080. [\[CrossRef\]](#) [\[PubMed\]](#)
- Kang, D.; Zhou, Y.; Yi, W.; Yang, C.; Guo, J.; Shi, Y.; Zhang, S.; Wang, Z.; Zhang, C.; Jiang, S.; et al. Superconductivity emerging from a suppressed large magnetoresistant state in tungsten ditelluride. *Nat. Commun.* **2015**, *6*, 7804. [\[CrossRef\]](#)
- Wu, Y.; Jo, N.H.; Ochi, M.; Huang, L.; Mou, D.; Bud'ko, S.L.; Canfield, P.; Trivedi, N.; Arita, R.; Kaminski, A. Temperature-Induced Lifshitz Transition in WTe₂. *Phys. Rev. Lett.* **2015**, *115*, 166602. [\[CrossRef\]](#)
- Zhu, Z.; Lin, X.; Liu, J.; Fauqué, B.; Tao, Q.; Yang, C.; Shi, Y.; Behnia, K. Quantum oscillations, thermoelectric coefficients, and the fermi surface of semimetallic WTe₂. *Phys. Rev. Lett.* **2015**, *114*, 176601. [\[CrossRef\]](#)

18. Tang, S.; Zhang, C.; Wong, D.; Pedramrazi, Z.; Tsai, H.Z.; Jia, C.; Moritz, B.; Claassen, M.; Ryu, H.; Kahn, S.; et al. Quantum spin Hall state in monolayer 1T'-WTe₂. *Nat. Phys.* **2017**, *13*, 683–687. [[CrossRef](#)]
19. Xia, F.; Wang, H.; Xiao, D.; Dubey, M.; Ramasubramaniam, A. Two-dimensional material nanophotonics. *Nat. Photonics* **2014**, *8*, 899–907. [[CrossRef](#)]
20. Reserbat-Plantey, A.; Epstein, I.; Torre, I.; Costa, A.T.; Gonçalves, P.A.D.; Mortensen, N.A.; Polini, M.; Song, J.C.W.; Peres, N.M.R.; Koppens, F.H.L. Quantum Nanophotonics in Two-Dimensional Materials. *ACS Photonics* **2021**, *8*, 85–101. [[CrossRef](#)]
21. Ling, H.; Li, R.; Davoyan, A.R. All van der Waals Integrated Nanophotonics with Bulk Transition Metal Dichalcogenides. *ACS Photonics* **2021**, *8*, 721–730. [[CrossRef](#)]
22. Ermolaev, G.A.; Grudin, D.V.; Stebunov, Y.V.; Voronin, K.V.; Kravets, V.G.; Duan, J.; Mazitov, A.B.; Tselikov, G.I.; Bylinkin, A.; Yakubovskiy, D.I.; et al. Giant optical anisotropy in transition metal dichalcogenides for next-generation photonics. *Nat. Commun.* **2021**, *12*, 854. [[CrossRef](#)]
23. Green, T.D.; Baranov, D.G.; Munkhbat, B.; Verre, R.; Shegai, T.; Käll, M. Optical material anisotropy in high-index transition metal dichalcogenide Mie nanoresonators. *Optica* **2020**, *7*, 680. [[CrossRef](#)]
24. Singh, A.; Jo, S.S.; Li, Y.; Wu, C.; Li, M.; Jaramillo, R. Refractive Uses of Layered and Two-Dimensional Materials for Integrated Photonics. *ACS Photonics* **2020**, *7*, 3270–3285. [[CrossRef](#)]
25. Maurya, S.; Nyman, M.; Kaivola, M.; Shevchenko, A. Highly birefringent metamaterial structure as a tunable partial polarizer. *Opt. Express* **2019**, *27*, 27335. [[CrossRef](#)]
26. Ghosh, G. Dispersion-equation coefficients for the refractive index and birefringence of calcite and quartz crystals. *Opt. Commun.* **1999**, *163*, 95–102. [[CrossRef](#)]
27. Pochi, Y.; Gu, C. *Optics of Liquid Crystal Displays*, 2nd ed.; John Wiley & Sons, Inc.: Hoboken, NJ, USA, 2009.
28. Ross, A.M.; Paternò, G.M.; Dal Conte, S.; Scotognella, F.; Cinquanta, E. Anisotropic Complex Refractive Indices of Atomically Thin Materials: Determination of the Optical Constants of Few-Layer Black Phosphorus. *Materials* **2020**, *13*, 5736. [[CrossRef](#)]
29. Banai, R.E.; Burton, L.A.; Choi, S.G.; Hofherr, F.; Sorgenfrei, T.; Walsh, A.; To, B.; Cröll, A.; Brownson, J.R.S. Ellipsometric characterization and density-functional theory analysis of anisotropic optical properties of single-crystal α -SnS. *J. Appl. Phys.* **2014**, *116*, 013511. [[CrossRef](#)]
30. Shubnic, A.A.; Polozkov, R.G.; Shelykh, I.A.; Iorsh, I.V. High refractive index and extreme biaxial optical anisotropy of rhenium diselenide for applications in all-dielectric nanophotonics. *Nanophotonics* **2020**, *9*, 4737–4742. [[CrossRef](#)]
31. Homes, C.C.; Ali, M.N.; Cava, R.J. Optical properties of the perfectly compensated semimetal WTe₂. *Phys. Rev. B Condens. Matter Mater. Phys.* **2015**, *92*, 161109. [[CrossRef](#)]
32. Song, Q.; Pan, X.; Wang, H.; Zhang, K.; Tan, Q.; Li, P.; Wan, Y.; Wang, Y.; Xu, X.; Lin, M.; et al. The In-Plane Anisotropy of WTe₂ Investigated by Angle-Dependent and Polarized Raman Spectroscopy. *Sci. Rep.* **2016**, *6*, 29254. [[CrossRef](#)]
33. Politano, A.; Viti, L.; Vitiello, M.S. Optoelectronic devices, plasmonics, and photonics with topological insulators. *APL Mater.* **2017**, *5*, 35504. [[CrossRef](#)]
34. Stauber, T. Plasmonics in Dirac systems: From graphene to topological insulators. *J. Phys. Condens. Matter* **2014**, *26*, 123201. [[CrossRef](#)] [[PubMed](#)]
35. Stauber, T.; Gómez-Santos, G.; Brey, L. Plasmonics in Topological Insulators: Spin-Charge Separation, the Influence of the Inversion Layer, and Phonon-Plasmon Coupling. *ACS Photonics* **2017**, *4*, 2978–2988. [[CrossRef](#)]
36. Popescu, A.; Pertsova, A.; Balatsky, A.V.; Woods, L.M. Optical Response of MoTe₂ and WTe₂ Weyl Semimetals: Distinguishing between Bulk and Surface Contributions. *Adv. Theory Simul.* **2020**, *3*, 1900247. [[CrossRef](#)]
37. Domozhirova, A.N.; Makhnev, A.A.; Shreder, E.I.; Naumov, S.V.; Lukoyanov, A.V.; Chistyakov, V.V.; Huang, J.C.A.; Semiannikova, A.A.; Korenistov, P.S.; Marchenkov, V.V. Electronic properties of WTe₂ and MoTe₂ single crystals. In Proceedings of the Journal of Physics: Conference Series, Ekaterinburg, Russia, 19–20 July 2019; Institute of Physics Publishing: Tokyo, Japan, 2019; Volume 1389, p. 12149.
38. Tan, C.; Yue, Z.; Dai, Z.; Bao, Q.; Wang, X.; Lu, H.; Wang, L. Nanograting-assisted generation of surface plasmon polaritons in Weyl semimetal WTe₂. *Opt. Mater.* **2018**, *86*, 421–423. [[CrossRef](#)]
39. Wang, C.; Huang, S.; Xing, Q.; Xie, Y.; Song, C.; Wang, F.; Yan, H. Van der Waals thin films of WTe₂ for natural hyperbolic plasmonic surfaces. *Nat. Commun.* **2020**, *11*, 1158. [[CrossRef](#)]
40. Wang, H.; Low, T. Hyperbolicity in two-dimensional transition metal ditellurides induced by electronic bands nesting. *Phys. Rev. B* **2020**, *102*, 241104. [[CrossRef](#)]
41. Torbatian, Z.; Novko, D.; Asgari, R. Tunable Low-Loss Hyperbolic Plasmon Polaritons in a Td—WTe₂ Single Layer. *Phys. Rev. Appl.* **2020**, *14*, 044014. [[CrossRef](#)]
42. Koo, J.; Jhon, Y.I.; Park, J.; Lee, J.; Jhon, Y.M.; Lee, J.H. Near-Infrared Saturable Absorption of Defective Bulk-Structured WTe₂ for Femtosecond Laser Mode-Locking. *Adv. Funct. Mater.* **2016**, *26*, 7454–7461. [[CrossRef](#)]
43. Chen, L.; Li, X.; Zhang, H.; Xia, W. Passively Q-switched 1989 μ m all-solid-state laser based on a WTe₂ saturable absorber. *Appl. Opt.* **2018**, *57*, 10239. [[CrossRef](#)]
44. Wang, J.; Jiang, Z.; Chen, H.; Li, J.; Yin, J.; Wang, J.; He, T.; Yan, P.; Ruan, S. Magnetron-sputtering deposited WTe₂ for an ultrafast thulium-doped fiber laser. *Opt. Lett.* **2017**, *42*, 5010. [[CrossRef](#)] [[PubMed](#)]
45. Naylor, C.H.; Parkin, W.M.; Gao, Z.; Kang, H.; Noyan, M.; Wexler, R.B.; Tan, L.Z.; Kim, Y.; Kehayias, C.E.; Streller, F.; et al. Large-area synthesis of high-quality monolayer 1T'-WTe₂ flakes. *2D Mater.* **2017**, *4*, 021008. [[CrossRef](#)] [[PubMed](#)]

46. Walsh, L.A.; Yue, R.; Wang, Q.; Barton, A.T.; Addou, R.; Smyth, C.M.; Zhu, H.; Kim, J.; Colombo, L.; Kim, M.J.; et al. WTe₂ thin films grown by beam-interrupted molecular beam epitaxy. *2D Mater.* **2017**, *4*, 025044. [[CrossRef](#)]
47. Wang, D.; Luo, F.; Lu, M.; Xie, X.; Huang, L.; Huang, W. Chemical Vapor Transport Reactions for Synthesizing Layered Materials and Their 2D Counterparts. *Small* **2019**, *15*, 1804404. [[CrossRef](#)]
48. Hansen, F.; Wels, M.; Froeschke, S.; Popov, A.; Wolf, D.; Büchner, B.; Schmidt, P.; Hampel, S. Thermodynamic Evaluation and Chemical Vapor Transport of Few-Layer WTe₂. *Cryst. Growth Des.* **2020**, *20*, 7341–7349. [[CrossRef](#)]
49. Predel, B. Te-W (Tellurium-Tungsten): Datasheet from Landolt-Börnstein—Group IV Physical Chemistry. In *Pu-Re-Zn-Zr*; Springer: Berlin/Heidelberg, Germany, 2005; Volume 5, pp. 1–2. [[CrossRef](#)]
50. Hou, F.; Zhang, D.; Sharma, P.; Singh, S.; Wu, T.; Seidel, J. Oxidation Kinetics of WTe₂ Surfaces in Different Environments. *ACS Appl. Electron. Mater.* **2020**, *2*, 2196–2202. [[CrossRef](#)]
51. Ye, F.; Lee, J.; Hu, J.; Mao, Z.; Wei, J.; Feng, P.X.-L. Environmental Instability and Degradation of Single- and Few-Layer WTe₂ Nanosheets in Ambient Conditions. *Small* **2016**, *12*, 5802–5808. [[CrossRef](#)]
52. Momma, K.; Izumi, F. VESTA 3 for three-dimensional visualization of crystal, volumetric and morphology data. *J. Appl. Crystallogr.* **2011**, *44*, 1272–1276. [[CrossRef](#)]
53. Brown, B.E. The crystal structures of WTe₂ and high-temperature MoTe₂. *Acta Crystallogr.* **1966**, *20*, 268–274. [[CrossRef](#)]
54. Jiang, Y.C.; Gao, J.; Wang, L. Raman fingerprint for semi-metal WTe₂ evolving from bulk to monolayer. *Sci. Rep.* **2016**, *6*, 19624. [[CrossRef](#)] [[PubMed](#)]
55. Larsen, G.K.; Zhao, Y. Extracting the anisotropic optical parameters of chiral plasmonic nanostructured thin films using generalized ellipsometry. *Appl. Phys. Lett.* **2014**, *105*, 071109. [[CrossRef](#)]
56. Fujiwara, H. *Spectroscopic Ellipsometry: Principles and Applications*; John Wiley & Sons: Chichester, UK, 2007; ISBN 978-0-470-01608-4.
57. Jellison, G.E.; Modine, F.A. Parameterization of the optical functions of amorphous materials in the interband region. *Appl. Phys. Lett.* **1996**, *69*, 371–373. [[CrossRef](#)]
58. Atuchin, V.V.; Golyashov, V.A.; Kokh, K.A.; Korolkov, I.V.; Kozhukhov, A.S.; Kruchinin, V.N.; Loshkarev, I.D.; Pokrovsky, L.D.; Prosvirin, I.P.; Romanyuk, K.N.; et al. Crystal growth of Bi₂Te₃ and noble cleaved (0001) surface properties. *J. Solid State Chem.* **2016**, *236*, 203–208. [[CrossRef](#)]
59. Atuchin, V.V.; Golyashov, V.A.; Kokh, K.A.; Korolkov, I.V.; Kozhukhov, A.S.; Kruchinin, V.N.; Makarenko, S.V.; Pokrovsky, L.D.; Prosvirin, I.P.; Romanyuk, K.N.; et al. Formation of Inert Bi₂Se₃(0001) Cleaved Surface. *Cryst. Growth Des.* **2011**, *11*, 5507–5514. [[CrossRef](#)]
60. Atuchin, V.V.; Bereznaya, S.A.; Beisel, N.F.; Korotchenko, Z.V.; Kruchinin, V.N.; Pokrovsky, L.D.; Saprykin, A.I.; Sarkisov, S.Y. Growth, chromium distribution and electrical properties of GaSe:Cr single crystals. *Mater. Chem. Phys.* **2014**, *146*, 12–17. [[CrossRef](#)]
61. Ermolaev, G.A.; Yakubovsky, D.I.; Stebunov, Y.V.; Arsenin, A.V.; Volkov, V.S. Spectral ellipsometry of monolayer transition metal dichalcogenides: Analysis of excitonic peaks in dispersion. *J. Vac. Sci. Technol. B* **2020**, *38*, 014002. [[CrossRef](#)]
62. Lv, H.Y.; Lu, W.J.; Shao, D.F.; Liu, Y.; Tan, S.G.; Sun, Y.P. Perfect charge compensation in WTe₂ for the extraordinary magnetoresistance: From bulk to monolayer. *EPL* **2015**, *110*, 37004. [[CrossRef](#)]
63. Toudert, J.; Serna, R. Interband transitions in semi-metals, semiconductors, and topological insulators: A new driving force for plasmonics and nanophotonics. *Opt. Mater. Express* **2017**, *7*, 2299–2325. [[CrossRef](#)]